Available online at www.sciencedirect.com
ScienceDirect
Journal of Nuclear Materials 361 (2007) 127–140
journal of nuclear materials
www.elsevier.com/locate/jnucmat

Kinetic Monte Carlo modeling of cascade aging and damage accumulation in Fe–Cu alloys

P.R. Monasterio [a], B.D. Wirth [a,*], G.R. Odette [b]

[a] Nuclear Engineering Department, University of California Berkeley, MC 1730, Berkeley, CA 94720, United States
[b] Mechanical and Environmental Engineering, University of California Santa Barbara, Santa Barbara, CA 93106, United States

Abstract

Irradiation embrittlement in nuclear reactor pressure vessel steels results from the hardening produced by a high number density of nanometer scale features. This paper describes a kinetic lattice Monte Carlo model to simulate the cascade aging and damage accumulation of neutron irradiated Fe–Cu alloys, including new algorithms to introduce additional displacement damage, including self-interstitial atom–vacancy recombination, and to introduce a flux of diffusing vacancies due to the supersaturated vacancy concentrations under irradiation. The results of initial KLMC simulations of damage accumulation in an Fe–0.3% Cu alloy at 290 °C and 10^{-11} dpa/s are presented and reveal the continuous formation and dissolution of three-dimensional vacancy–Cu clusters from the remnants of the vacancy-rich displacement cascade core, in addition to the formation of a high number density of copper clusters that grow with increasing irradiation dose. To our knowledge, this represents the first kinetic Monte Carlo model simulation that captures both Cu precipitate formation and vacancy–Cu cluster formation, as is experimentally observed. KLMC simulation results that investigate the effect of increasing irradiation dose rate from 10^{-13} to 10^{-9} dpa/s are also presented. Future modeling efforts will evaluate the effect of the model parameters, perform multiple simulations to provide statistical evaluation of the copper precipitate and vacancy–Cu cluster evolutions, and quantitatively compare the results to available experimental data.

1. Introduction

Western reactor pressure vessel (RPV) steels are fabricated from quenched and tempered low-alloy C–Mn–Si–Mo–Ni bainitic steels, and often contain copper and phosphorous as trace impurities. RPVs operate at temperatures around 290 °C and are exposed to fast neutron fluences from about 1–10×10^{23} nm^{-2} over a 40–60 year service life, corresponding to a maximum damage dose less than ≈0.15 displacements per atom (dpa) and damage dose rates on the order of $0.8–8 \times 10^{-11}$ dpa/s [1–3]. However, even this relatively low dose is sufficient to produce severe embrittlement, where embrittlement is characterized by an upward shift in the transition temperature (ΔT) between the more brittle cleavage and more ductile microvoid coalescence fracture regimes, with ΔTs in excess of 300 °C in some cases [2].

* Corresponding author. Tel.: +1 510 642 5341; fax: +1 510 643 9685.
E-mail address: bdwirth@nuc.berkeley.edu (B.D. Wirth).

0022-3115/$ - see front matter © 2007 Elsevier B.V. All rights reserved.
doi:10.1016/j.jnucmat.2006.12.022

Embrittlement is primarily the result of irradiation hardening, or yield strength increases, and is controlled by a complex combination of variables, including the neutron flux, fluence and energy spectrum, the irradiation temperature (irradiation variables), and the alloy's starting microstructure and composition (material variables) [1–6]. Important compositional variables include Cu (0.02–0.5 wt%), Ni (0.2–2 wt%) and Mn (0.3–2 wt%), while P (0.005–0.040 wt%) and Si (0.2–0.7 wt%) generally play secondary roles. Although Cu impurity levels may be as high as 0.5% in RPV welds and forgings, pre-precipitation of copper during post-weld heat treatment typically limits the maximum effective concentration to about 0.3 wt% [3]. The principal source of irradiation hardening is the formation of high number densities of nanometer-sized irradiation-induced precipitates and so-called matrix features, which impede the motion of dislocations [1–6]. In Cu-bearing steels, the nanometer-sized precipitates are copper rich (CRPs), but also contain Ni, Mn and Si, and rapidly form due to radiation-enhanced solute diffusion. Mn–Ni rich precipitates (MNPs) containing a range of Cu, form at high alloy Mn and Ni levels, and are promoted by lower irradiation temperatures (<290 °C) and Cu contents [2,7]. Smaller, so-called matrix features, believed to be vacancy–solute (e.g., Cu, Mn, Ni and Si) cluster complexes, or their solute remnants, also contribute to hardening, even in alloys with low or no copper [1–3,5,8].

The nanometer precipitates have been characterized by a combination of experimental techniques, including small angle neutron scattering (SANS) [2,9–12], atom probe field ion microscopy (APFIM) [12–15], combined electrical resistance Seebeck coefficient measurements (RSC) [16,17], and recently, positron annihilation spectroscopy (PAS) [11,18–22], as a function of steel composition, heat treatment, irradiation temperature, neutron flux and fluence. In general, the results derived from the different techniques are in good agreement, although some questions remain regarding the composition of the precipitates, particularly with respect to their possible Fe content [12]. The matrix features have been primarily identified and characterized by a combination of post-irradiation annealing and microhardness measurements [23], in addition to more recent positron annihilation spectroscopy measurements [20–22].

While a significant experimental database on the nanometer precipitates and the matrix features exists, a more detailed atomic scale understanding is required to better underpin predictive embrittlement models. Developing such models is a great challenge, in part because the relevant phenomena encompass a wide range of length and time scales [4,5,8,24], and perhaps more importantly, because embrittlement is controlled by the synergistic interaction of a large number of irradiation variables [1–3]. As pointed out by Odette [1,4,8], increased radiation damage dose rate (neutron flux) can either increase, decrease or not influence RPV embrittlement, depending on the specific combination of irradiation temperature, dose rate, dose and alloy Cu and Ni content. Many other examples of the complex and synergistic dependence of RPV embrittlement also exist and emphasize the need for physically-based embrittlement models. Previous theoretical modeling, using either rate theory or atomistic kinetic Monte Carlo approaches, have been successful in predicting aspects of the precipitate or matrix feature evolution, but have not yet been able to describe the complete and fully coupled evolution of nanostructural features in irradiated RPV steels.

Odette and co-workers have developed continuum models of both vacancy and Cu clustering based on integrating discrete sets of master equations that describe the nucleation, growth and coarsening evolution of precipitates and nanovoid complexes. These models partially rationalize the observed irradiation temperature dependence of matrix features, but were not able to fully explain the sensitivity to irradiation flux [2–4,6,8]. Wirth and Odette [25], and Becquart and co-workers [26] have developed kinetic lattice Monte Carlo (KLMC) models of the time and spatial dependent evolution of displacement damage in Fe–Cu alloys. These Monte Carlo models predict the formation and evolution of vacancy–Cu atom matrix features, which are reasonably consistent with the matrix features observed in irradiated Fe–Cu alloys by PAS [11,21,22]. However, these KLMC models were not able to describe the formation of both the vacancy–Cu clusters and the Cu-precipitates, nor the dependencies on the irradiation variables.

The objective of this work is to extend the KLMC model of Wirth and Odette [25] in order to simulate the formation and evolution of both nanometer copper precipitates and matrix features in the form of vacancy–copper clusters. The present paper provides a detailed description of the modeling approach and the new algorithms, and then

provides an illustrative example of copper precipitate formation and growth, in addition to the transient evolution of vacancy–copper clusters predicted by the KLMC model. A more detailed presentation of the simulation results, including a complete statistical analysis of the precipitate and matrix feature populations and their dependence on the parameters of the model, will be published in the future. In this paper, Section 2 describes the KLMC model and the algorithms developed to include long-range defect migration and additional cascade damage at the appropriate dose rate. Section 3 presents the results and discussion associated with initial simulations in an Fe–0.3% Cu alloy at irradiation temperatures and dose rates relevant to RPV embrittlement. Section 4 summarizes the paper and discusses the next steps required to further develop the KLMC model into a predictive multiscale model of irradiation-induced RPV embrittlement.

2. Kinetic lattice Monte Carlo modeling approach

The KLMC model of cascade aging and damage accumulation has been developed within a multiscale framework to understand and simulate RPV irradiation embrittlement. The approach combines an MD database of primary damage production with two separate kinetic Monte Carlo (KMC) simulation techniques that follow the isolated and clustered self-interstitial atom (SIA) diffusion away from a cascade, and the subsequent vacancy and solute atom evolution. Separation of the vacancy and SIA cluster diffusional time scales naturally leads to the nearly independent evolution of these two populations, at least for the relatively low dose rates that characterize RPV embrittlement [1–5].

The relatively short time (~100 ns at 290 °C) evolution of the cascade is modeled using 'defect'-oriented KMC [27,28]. This model uses the positions of vacancy and SIA defects produced in cascades obtained from an MD database provided by Stoller [29–31], and allows for additional SIA/vacancy recombination within the cascade volume and the migration of SIA and SIA clusters away from the cascade to annihilate at system sinks. During this 'defect' KMC, the time duration is too short for significant vacancy migration and thus, the SIA/SIA clusters are the only diffusing defects. The 'defect' KMC simulations, which are described in detail elsewhere [28,32], thus provide a database of initially 'aged' cascades for longer time KLMC cascade aging and damage accumulation simulations.

2.1. KLMC vacancy–atom exchange algorithm

The KLMC model simulates cascade aging and damage evolution in dilute Fe–Cu alloys by following vacancy–nearest neighbor atom exchanges on a bcc lattice, beginning from the spatial vacancy population produced in 'aged' high-energy displacement cascades to the ultimate annihilation of vacancies at the simulation cell boundary, and including the introduction of new cascade damage and fluxes of mobile point defects. The KLMC boundary conditions remove (annihilate) a vacancy upon contact, and other than vacancy clusters the cell boundary is the only explicit vacancy sink included in this model. Thus vacancies either cluster or diffuse through the simulation volume until reaching the cell boundary where they annihilate. Within a cluster, individual vacancies maintain their identity. Vacancy–solute clusters can grow by absorbing single vacancies, which may be emitted from other clusters, or by coalescence of mobile clusters, and can shrink by emitting individual vacancies.

The potential energy of the local vacancy–Cu–Fe environment determines the relative vacancy jump probability to each of the eight possible nearest neighbors in the bcc lattice. The unrelaxed Fe–Cu–vacancy lattice energetics are described using Finnis–Sinclair N-body type potentials. The iron and copper potentials are from Finnis and Sinclair [33] and Ackland et. al. [34], respectively; and the iron–copper potential was developed by fitting the dilute heat of solution for copper in iron, the copper–vacancy binding energy and the iron–copper {1 1 0} interface energy, as described elsewhere [35].

In the KLMC model, the specific jump of each vacancy in the system is based on a Metropolis random number test [36], and the time (Δt_{KLMC}) associated with a Monte Carlo sweep is calculated from the vacancy with the highest total probability. The jump probability for each vacancy (i) to exchange with a nearest neighbor position (j), is calculated using a Boltzmann factor and summed over the eight nearest neighbor positions to obtain the total probability (P_i) for each vacancy as:

$$P_i = \sum_{j=1}^{8} \exp\left(-\frac{\Delta E}{kT}\right); \quad \Delta E = E^* + \frac{\Delta E_{i-j}}{2}, \tag{1}$$

where ΔE is the activation energy for the vacancy jump, which is set equal to a constant saddle point energy (E^*) plus one half of the potential energy change (ΔE_{i-j}) associated with the exchange of the vacancy from position i to j. Within a vacancy cluster, each vacancy maintains its identity, and while vacancy–vacancy exchanges are not allowed, the cluster can migrate through the collective motion of its constituent vacancies. The saddle point energy (E^*) is set to 0.9 eV, which is the activation energy for vacancy exchange in pure iron calculated with the Finnis–Sinclair Fe potential [33]. The modification of the jump activation energy by $\Delta E_{i-j}/2$ represents an attempt to model the effect of the local environment on the jump frequencies. Indeed, detailed molecular statics calculations suggest that this represents an upper-bound influence of the effect [35], although the detailed balance of vacancy jumps to neighboring positions is maintained by this assumption.

The time (Δt_{KLMC}) of each KLMC sweep (or step) is determined by $\Delta t_{\mathrm{KLMC}} = (\nu P_{\max})^{-1}$, where $P_{\max}$ is the highest total probability of the vacancy population, and ν is an effective attempt frequency. In this work, $\nu = 10^{14}\ \mathrm{s}^{-1}$, to account for the intrinsic vibrational frequency and entropic effects associated with vacancy formation and migration, as used in the previous KLMC model by Wirth and Odette [25]. As mentioned, the possible exchange of every vacancy (i) to a nearest neighbor is determined by a Metropolis random number test [36] of the relative vacancy jump probability ($P_i/P_{\max}$) during each Monte Carlo sweep. Thus at least one, and often multiple, vacancy jumps occur during each Monte Carlo sweep. Further, since the total probability associated with a vacancy jump depends on the local environment, the intrinsic timescale (Δt_{KLMC}) changes as a function of the number and spatial distribution of the vacancy population, as well as the spatial arrangement of the Cu atoms in relation to the vacancies.

As an example, the evolution of the vacancy population from a single cascade begins with very short time increments ($\sim$0.1 μs) as the unbound and isolated vacancies diffuse, but increases once isolated vacancies no longer exist because of clustering with other vacancies or copper (binding increases ΔE and therefore decreases P_i because of the dependence on the local potential energy), or annihilation at the cell boundary. The time increment increases as the evolution is then governed by the migration and dissolution of small, relatively weakly bound vacancy–solute complexes, and then increases further when only relatively large vacancy cluster complexes form. Since vacancy cluster mobility decreases rapidly with size, whereas vacancy binding energy increases with cluster size; the efficiency of the KLMC simulation in terms of the overall system evolution (vacancy and Cu atom diffusion) decreases dramatically when the vacancy population only involves clusters larger than about seven to ten vacancies. In such a case, a weakly bound vacancy is emitted by a one nearest neighbor distance jump from the cluster(s), only to immediately return on the next Monte Carlo sweep. This process continually repeats, often accompanied by fluctuations in the cluster shape. Since these cluster sizes are generally well below the critical size of growing voids, they are thermodynamically unstable and should ultimately dissolve.

Thus, Wirth and Odette [25] devised a 'pulsing algorithm' approach to accelerate vacancy emission from large vacancy clusters and 'jump' the KLMC simulation forward in time to simulate the next stage of damage accumulation. As described previously [25], the algorithm is invoked after N 'inefficient' sweeps, i.e. steps with no free vacancy movement, where N is typically on the order of 600, and involves a single step with an increased temperature to identify the least strongly bound vacancy (or vacancies), and to establish an emission trajectory away from the cluster. Three additional steps then force the vacancy (or vacancies) along the identified emission trajectory at the original simulation temperature. The objective of these three jumps is to obtain a roughly equal probability for the emitted vacancies to return to the original cluster or to diffuse away. The goal of the pulsing algorithm is to jump forward in time to the next rate-limiting process controlling the overall microstructural evolution. Ideally, this will improve the computational efficiency by skipping a large number of inefficient KLMC steps that do not involve significant evolution of the vacancy and solute atom populations. The overall time step during the pulse-annealing algorithm (Δt_{PA}) is obtained by

$$\Delta t_{\mathrm{PA}} = \Delta t_{\mathrm{KLMC}} + \Delta t_1 + \Delta t_2 + \Delta t_3;$$
$$\Delta t_i = \frac{1}{\nu P_{\mathrm{emitted,v}}}, \tag{2}$$

where Δt_{KLMC} specifies the time associated with the first jump, which is calculated from the highest vacancy probability (summed over all 8 possible

jumps) at the original simulation temperature and Δt_i are calculated from the probability of the specific jump trajectory for each of the three additional jumps away from the vacancy cluster.

In addition to the vacancy evolution from an isolated cascade, damage accumulation is modeled by including algorithms to introduce additional vacancies at an appropriate displacement rate along with a diffusing flux of vacancies from the super-saturated vacancy population during irradiation.

2.2. KLMC displacement damage introduction algorithm

Damage accumulation is modeled by introducing 'aged' cascades into either the main simulation volume (of dimension $100a_0 \times 100a_0 \times 100a_0$) or one of the twenty-six corresponding nearest neighbor volumes. The nearest neighbor volumes are effectively coupled to the main simulation volume to provide diffusing fluxes of vacancy and SIAs as they escape (diffuse away) from the cascade. The rate of displacement damage introduction is specified by the neutron scattering rate (collisions per atom per second) as:

$$\mathrm{Rate}_{\mathrm{scattering}} = \sigma_s \phi, \tag{3}$$

where σ_s is the neutron scattering cross-section, taken to be 3 barns, and ϕ is the fast ($E > 1$ MeV) neutron flux. The kinetic energy of the scattered lattice recoil atom, T, is determined for each scattering collision, by random number sampling from the normalized recoil spectrum obtained from the SPECTER code [30,37] for an RPV in a pressurized light water reactor neutron energy spectrum. Table 1 presents the recoil (cascade energy) spectra used in this work. The dose is updated by adding the incremental dose associated with the scattering event of recoil energy T, using the Norgett–Robinson–Torrens expression [38] for the number of displaced atoms, as

$$\mathrm{dose} = \mathrm{dose} + \frac{\left(\frac{0.8 * T_{\mathrm{recoil}}}{2E_{\mathrm{d}}}\right)}{N(\mathrm{total\ atoms} = 27 * 2 \times 10^6)}, \tag{4}$$

where the displacement energy E_{d} is the recommended value of 40 eV for Fe and RPV steels [39].

The position of the lattice recoil (of kinetic energy T) and thus the center of mass of the displacement cascade is chosen randomly, and can be within either the main simulation volume or in one of the twenty-six nearest neighbor volumes. If the cascade (lattice recoil) is placed into the main simulation cell (with probability of 1/27), the vacancy positions from an aged cascade of recoil energy T are introduced into the simulation volume from the 'aged' cascade database. SIA and SIA cluster diffusion and evolution from this new cascade is not modeled explicitly, although recombination between pre-existing vacancies and the newly introduced cascade is modeled. This assumption neglects the possibility of copper diffusion by a SIA-mechanism. However, since Cu is an over-sized solute atom in the bcc Fe lattice, this is not expected to significantly contribute to Cu diffusion, as confirmed by molecular dynamics simulations [40].

The SIA population produced in each cascade, and correspondingly the recombination probability is treated in three populations, namely, single SIA, tri-SIA clusters and eight-member SIA clusters, as representative of the SIA cluster distribution produced in displacement cascades in Fe [29–31,41]. Based on MD simulations [5,42,43], the single and 3-SIA are assumed to migrate three-dimensionally, and the 8-SIA cluster is assumed to migrate one-dimensionally. The dimensionality of SIA/SIA cluster diffusion determines the effective recombination radius, r_0, with a vacancy. The assumed values of r_0 used in this work are $r_0 = 5a_0$ for single SIA, $r_0 = 3a_0$ for 3-SIA clusters and $r_0 = 2a_0$ for 8-SIA clusters, respectively. The probability of

Table 1
The normalized probability distribution function and the number of single SIA, 3-SIA and 8-SIA clusters for a given cascade (recoil) energy

Cascade energy (keV)	Recoil probability	Number of single SIA	Number of tri-SIA clusters	Number of 8-SIA clusters
0.1	0.148	1	0	0
0.5	0.185	4	0	0
1	0.185	3	1	0
5	0.259	8	1	1
20	0.148	24	6	2
40	0.074	27	10	4

vacancy–SIA recombination is calculated as the product of the recombination volume ($\propto r_0^3$) and the vacancy concentration per unit volume. As well, an additional conditional probability describes whether the recombination of 3- and 8-SIA clusters produces the annihilation of one, two or three vacancies. A conditional probability of 65% and 22% is assumed for single vacancy recombination, 33% and 35% for recombination of 2 vacancies, and 2% and 22% for recombination of 3 vacancies of the 3- and 8-SIA clusters, respectively. The number and size distribution of SIA for a given recoil energy are provided in Table 1, and were selected to be consistent with the MD displacement cascade database of Stoller [29–31].

If the cascade (lattice recoil) is introduced into the neighboring simulation volumes, then a flux of diffusing vacancies and SIAs is introduced into the main simulation volume. The SIA/SIA cluster population is again not modeled explicitly, although recombination with pre-existing vacancies is calculated based on the probability,

$$P_{\text{recombine}} = \frac{1}{6} * r_0^3 * C_{\text{v}} + \frac{5}{6} * \frac{1}{6} * r_0^3 * C_{\text{v}}, \tag{5}$$

where C_{v} is the vacancy concentration per unit volume in the main simulation cell, and the two terms of Eq. (5) are meant to account for the direct diffusion of the SIA/SIA cluster into the main simulation volume from the neighboring cell (probability = 1/6) and following initial diffusion into a different neighboring volume (probability = 5/6 * 1/6). The recombination radii and conditional vacancy recombination probabilities are the same as used for a cascade introduced within the main volume. Vacancies are introduced at a rate based on the probability of diffusion away from the cascade volume and into the main simulation volume, as:

$$P_{\text{vac,introduction}} = \frac{P_{\text{v,escape}}}{6} + \frac{5}{6} * \frac{1}{6} * (1 - P_{\text{v,escape}}), \tag{6}$$

where $P_{\text{v,escape}}$ is the probability that vacancies diffuse away from the cascade region before clustering. Again, the 1/6 and 5/36 values are introduced to account for the geometric dependence of vacancy diffusion into the main simulation volume. $P_{\text{v,escape}}$ should be a function of recoil (cascade) energy, however, it is assumed equal to 0.60 in this work, independent of recoil energy based on simulations of the aging evolution of isolated cascades [25].

2.3. KLMC vacancy flux introduction algorithm

The introduction of additional cascade damage and point defect fluxes from neighboring cascade volumes represents a first step towards incorporating the irradiation-induced defect concentrations and fluxes into the KLMC simulation. However, the rate of vacancy introduction described in Section 2.2 does not fully account for the point defect (vacancy) fluxes, because of the high vacancy sink strength in the KLMC simulation and because the damage introduction algorithm does not include a vacancy flux driven by the thermal emission (shrinkage) of cascade-induced vacancy clusters, nor fully treat the supersaturated vacancy concentration and corresponding long-range vacancy diffusion to sinks. Thus single vacancies are also introduced into the simulation based on an estimate of the supersaturated vacancy flux.

The rate of vacancy introduction is determined from the product of the cross-sectional surface area and the vacancy flux, as calculated from Fick's first law. The spatial concentration gradient is simply approximated as the difference between the thermodynamic equilibrium concentration and the steady-state vacancy concentration under irradiation, divided by a microstructural length scale, which is estimated based on the characteristic length between vacancy sinks. Thus,

$$R_{\text{vacancy,add}} = A_{\text{s}} * \left(-D_{\text{v}} \frac{(C_{\text{v}}^{\text{eq}} - C_{\text{v}}^{\text{ss}})}{L} \right), \tag{7}$$

where A_{s} is the surface area of the main simulation cell ($100a_0 \times 100a_0$), D_{v} is the vacancy diffusivity, C_{v}^{eq} is the thermodynamic equilibrium vacancy concentration and L is a characteristic length scale to linearize the concentration gradient. D_{v} and C_{v}^{eq} are calculated from the values of vacancy migration activation energy of 0.9 eV and formation energy of 1.7 eV, respectively obtained from the Finnis–Sinclair Fe potential [33]. The steady-state vacancy concentrations under irradiation have been estimated from standard rate theory. Vacancy introduction rates from 10^{-5} to $10^{-2}\,\text{s}^{-1}$ are obtained from Eq. (7) based on expected ranges for the dislocation density (10^{11}–$10^{15}\,\text{m}^{-2}$), grain size (10–1000 μm) and recombination radius ($2a_0$–$4a_0$) [44].

There are other approximations in the current KLMC simulation method that should be noted. First, the quantitative accuracy of the simulations depends on the validity of the interatomic potentials,

in particular in relation to the vacancy migration energy, the vacancy–Cu and vacancy–vacancy cluster binding energies and the Fe–Cu thermodynamics that are approximate at best. Indeed, recent ab initio calculations indicate the need to modify some of these parameters [45,46]. Also, a more rigorous residence time algorithm would provide a slightly better estimate of the absolute time scale. However, our simpler approach is believed to be a good qualitative approximation of cluster complex evolution and Cu precipitation during cascade aging and damage accumulation. In this regard, it should be noted that the physics dictating the evolution and ultimate fate of cascade vacancies primarily derives from their high degree of geometric correlation, rather than the exact kinetic sequence-of-events.

While significant work remains to refine the parameters and assess their adequacy in the current KLMC model (e.g., vacancy introduction rate, recombination radii, cascade escape probabilities, sink strengths, etc.), to perform multiple simulations to obtain statistics regarding the effect of key variables, and to extend the time/dose of the simulation; the initial results described in Section 3 do capture the combined evolution kinetics of the continuous formation and dissolution of three-dimensional vacancy–Cu clusters from the remnants of the vacancy-rich displacement cascade core, in addition to the formation of a high number density of copper clusters that grow with increasing irradiation dose. Future publications will provide a more detailed presentation of the effect of the model parameters on the precipitate and matrix feature populations.

3. Results and discussion

The KLMC simulations are performed in a randomly distributed Fe–0.3% Cu alloy at an irradiation temperature of 290 °C and started from the spatial distribution of vacancies from an 'initially aged' 20 keV displacement cascade. The rate of introducing new cascade damage is 1.13×10^{-5} cascades/s, a cascade vacancy escape probability of 0.60 and a vacancy introduction rate of 1×10^{-4} vacancies/s. Based on the recoil distribution provided in Table 1, the damage rate of this simulation is $\sim10^{-11}$ dpa/s. Thus a new cascade (with recoil energy from 100 eV to 40 keV) occurs within the simulated volume (a cube of ~86 nm edge length) every 8.8×10^{4} s (~1 day), while an individual vacancy diffuses into the simulation volume every 1×10^{4} s (~3 h). KLMC simulations have also been performed to study the effect of varying the cascade introduction rate from 1.13×10^{-3} to 1.13×10^{-7} cascades/s (dpa rates from 1×10^{-9} to 1×10^{-13} dpa/s). The simulated conditions should be compared to those experienced by RPVs in light water reactors, namely from 8×10^{-12}–8×10^{-11} dpa/s, and to model alloys irradiated in test reactors, which are in the range of 10^{-9}–10^{-10} dpa/s.

Figs. 1 and 2 show representative snapshots of the vacancy and Cu solute atom distributions as a function of time and dose at 290 °C. Note, only the Cu atoms which are part of vacancy or Cu atom clusters are presented in the figure. The main simulation volume consists of 2×10^{6} atoms ($100a_0\times100a_0\times100a_0$) of which 6000 atoms are Cu (0.3 atom%). Fig. 1 demonstrates the aging evolution of a single cascade (increasing time at fixed dose prior to introducing additional diffusing vacancies or new cascade), while Fig. 2 demonstrates the overall evolution with increasing time and dose. The aging of the single cascade is representative of the average behavior observed, although the number and size distribution of vacancy–Cu clusters does vary considerably from cascade to cascade. Further, Fig. 1 is representative of the results obtained with the previous KLMC models of Wirth and Odette [25] and Becquart and co-workers [26], which demonstrated the formation and subsequent dissolution of vacancy–Cu clusters. But Fig. 2 represents a significant extension of the previous work in regards to the size and number of Cu clusters formed.

Fig. 1(a) shows the initial vacancy configuration from an aged 20-keV cascade. Within 200 μs at 290 °C, the vacancies begin to diffuse and cluster, although no vacancies have yet reached the cell boundary to annihilate. Eleven (11) of the initial vacancies remain isolated, while thirteen (13) small vacancy clusters rapidly form within the initial cascade volume. The vacancy clusters range in size from two to six vacancies. At this stage, only two of the vacancy clusters are associated with copper atoms, a di-vacancy cluster with 1 Cu atom and a tetra-vacancy cluster with 2 Cu atoms. From 200 μs to 2 ms, the vacancy cluster population evolves by the diffusion of isolated vacancies through and away from the cascade region, and the emission and absorption of isolated vacancies in vacancy clusters, in addition to the diffusion of the small di-, tri- and tetra-vacancy clusters. Fig. 1(b) shows the configuration about 2 ms after the cascade. By this time, fourteen (14) of the original vacancies have diffused to

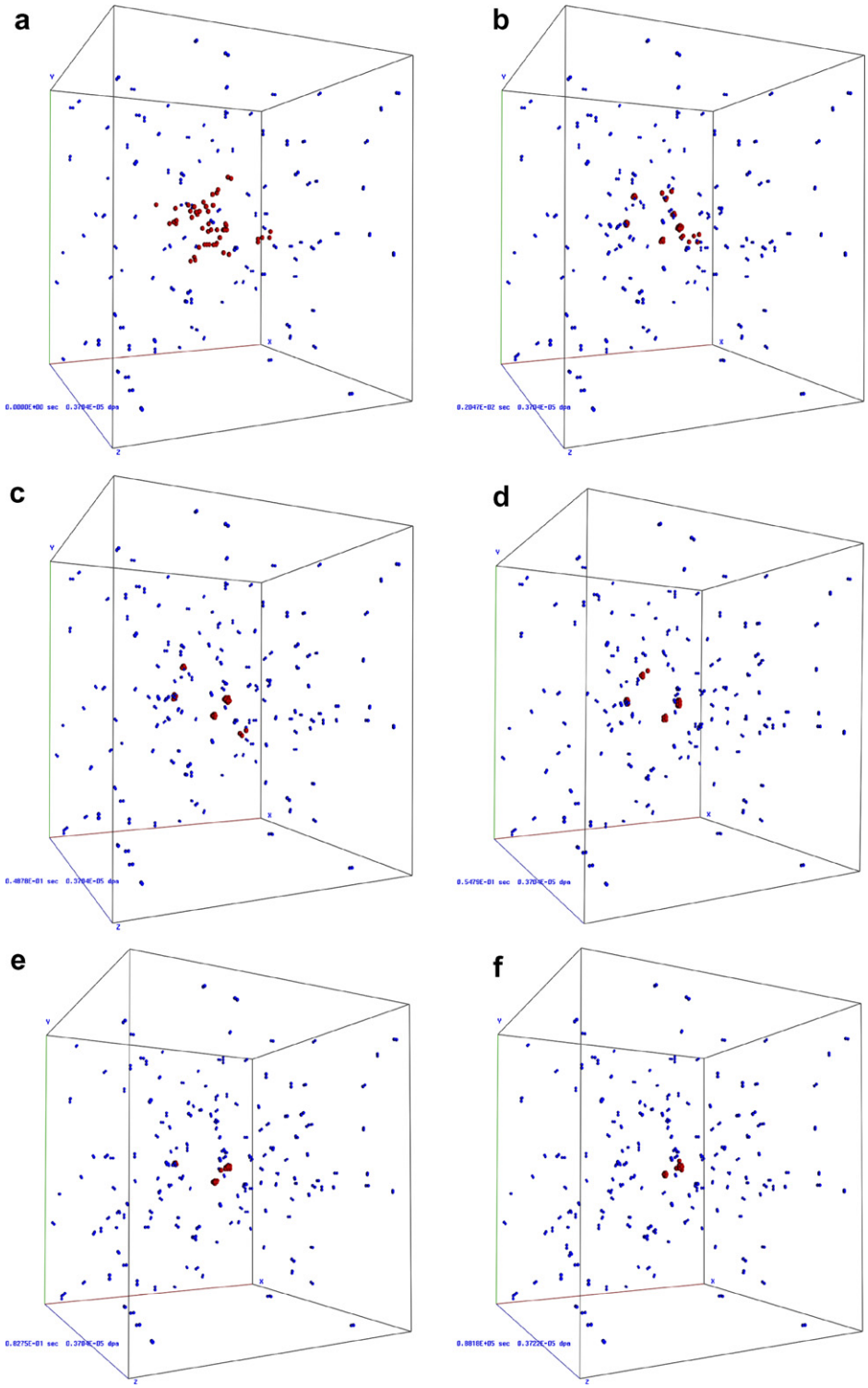

Fig. 1. Representative vacancy (red circles) and clustered Cu atom (blue circles) evolution in an Fe–0.3% Cu alloy during the aging of a single 20 keV displacement cascade, at (a) initial (200 ns), (b) 2 ms, (c) 48 ms, (d) 55 ms, (e) 83 ms, and (f) 24.5 h.

the cell boundary and annihilated, while 38 vacancies remain. The vacancy distribution includes six (6) isolated vacancies and seven (7) vacancy clusters, ranging in size from two di-vacancy clusters to a ten

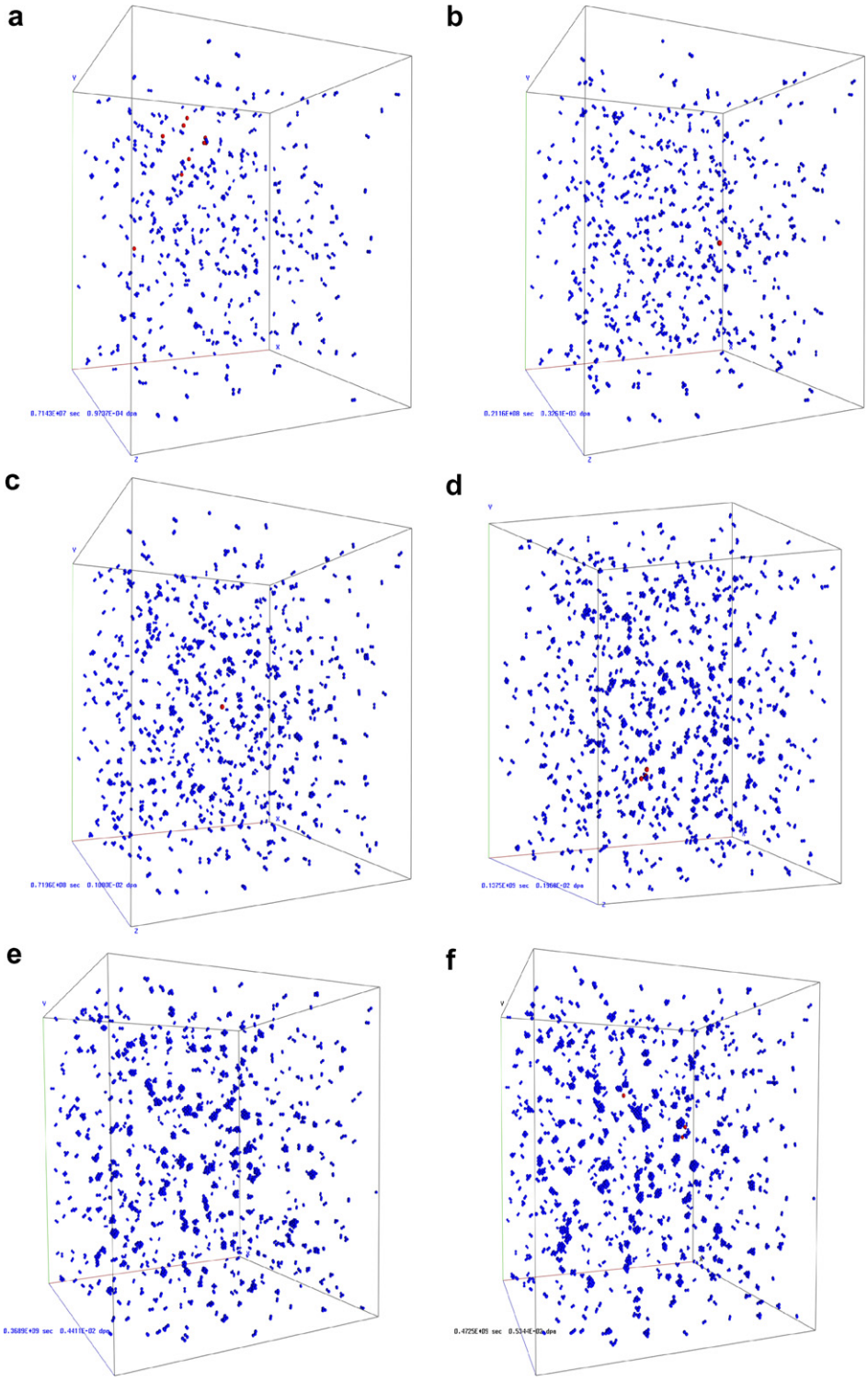

Fig. 2. Representative vacancy (red) and clustered Cu atom (blue) evolution in an Fe–0.3% Cu alloy with increasing dose at (a) 0.2 years (97 Mdpa), (b) 0.6 y (0.32 Mdpa), (c) 2.1 y (1.1 Mdpa), (d) 4.0 y (2.0 Mdpa), (e) 10.7 y (4.4 Mdpa), and (f) 13.7 y (5.3 Mdpa).

(10)-vacancy cluster. The number of non-isolated copper atoms has increased from 223 in the initial random distribution to 286 following the initial 2 ms of cascade aging.

The evolution from 2 to 48.8 ms involves the diffusion of isolated vacancies and di- and tri-vacancy clusters, along with the thermal emission of vacancies from the di- and tri-vacancy clusters. Over this time, 7 additional vacancies have diffused to the cell boundary and annihilated, and 20 additional Cu atoms have been incorporated into Cu or vacancy clusters. Fig. 1(c) shows the vacancy and Cu cluster population at 48.8 ms, which now consists of three (3) isolated vacancies and four (4) vacancy clusters, including a 4 V–1 Cu cluster, a 6 V–4 Cu cluster, a 7 V cluster and an 11 V–1Cu cluster. Fig. 1(d) and (e) show the vacancy and Cu cluster population at 54.8 and 82.8 ms, respectively. During this time the total number of vacancies has been further reduced from 31 to 21 of the original 52 vacancies, the vacancy cluster population has been reduced to three vacancy clusters (a 4 V–1 Cu, 7 V and 9 V–1 Cu) and 30 additional Cu atoms have incorporated into clusters because of vacancy exchanges.

Over times longer than 100 ms, the 4 V–1Cu atom cluster migrates a short distance on the order of 1 nm before shrinking by emitting vacancies, while the 7 V and 9 V–1 Cu cluster slowly evolve by local shape re-arrangements which produces only limited local diffusion. Both the 7 V and 9 V–1 Cu cluster are thermodynamically unstable in dilute Fe alloys at 290 °C and ultimately will shrink over longer times. The vacancy and Cu atom evolution in the KLMC model is now governed by the relative rate of vacancy cluster dissolution, as determined from the 'pulsing' algorithm, and the rate of new displacement damage and the diffusing supersaturated vacancy flux under irradiation. Fig. 1(f) shows the configuration about 8.8×10^4 s (~24 h) after the initial 20 keV cascade. Only 17 vacancies now exist in the cell, an isolated vacancy which entered the cell following escape from a 500 eV recoil introduced into a neighboring cell plus two vacancy clusters, consisting of 7 V–1 Cu and 9 V–1 Cu. 345 Cu atoms (of the initial 6000) have been removed from the supersaturated solution following the initial 24 h of evolution, mostly in the form of di- and tri-Cu atom clusters.

Fig. 2 shows the representative vacancy and (clustered) Cu atom microstructure evolution simulated by KLMC with increasing dose to 5.3 Mdpa at 290 °C at a dose rate of 10^{-11} dpa/s and a vacancy introduction rate of 10^{-4} s^{-1}. In this example, the dose (time) and number of vacancies and Cu cluster population should be considered representative, rather than absolute, and future simulations will quantify the statistical significance of the size distributions and validate the corresponding dose and times. Fig. 2(a) shows the configuration at about 0.1 Mdpa (0.097 Mdpa) and a time of 7.1×10^6 s (~82 days). Ten vacancies exist in the simulation cell, consisting of 8 isolated vacancies and one 2-V cluster, while 807 Cu atoms have been removed from solution in clusters, although the Cu cluster size distribution is clearly very fine. The majority of Cu clusters contain only 2 Cu atoms, while the largest cluster consists of only 5 Cu atoms. Fig. 2(b) shows the configuration at a dose of 0.33 Mdpa and time of 2.1×10^7 s (245 days). Only one vacancy exists in the simulation volume, while 1210 Cu atoms are now part of clusters, including twelve clusters containing 5 or more Cu atoms. Fig. 2(c) shows the evolution at 1 Mdpa and 7.2×10^7 s (~2.3 years). Again, only one vacancy exists in the simulation cell, while 1767 Cu atoms have been removed from supersaturated solution. A handful of well-formed spherical Cu clusters are visible, with the largest containing 13 Cu atoms. With increasing dose, the free Cu concentration in solution continues to decrease as Cu atoms join clusters and the average Cu cluster size grows. Fig. 2(d) and (e) show the clustered Cu atom population at about 2 and 4.4 Mdpa, respectively. The growth of the Cu clusters is clearly evident by comparing Fig. 2(d) and (e). At a dose of 4.4 Mdpa, forty-eight clusters contain more than 10 Cu atoms, and the largest cluster has 28 Cu atoms. The accumulated dose of 5.34 Mdpa is shown in Fig. 2(f). At this dose, more than 1/3 of the available Cu atoms have precipitated into clusters, the largest of which contains 42 Cu atoms, corresponding to a precipitate radius of ~0.5 nm.

Fig. 3 shows the size distribution of Cu atom clusters at 5.34 Mdpa, corresponding to the configuration shown in Fig. 2(f). The vast majority of the Cu-clusters consist of di-, tri-, tetra- and penta-Cu atom clusters. However, as shown in the inset to Fig. 3 and as visible in Fig. 2(f), a significant number of the Cu atom clusters contain more than 5 Cu atoms. Indeed, 29 clusters contain 15 or more Cu atoms (a number density of 1.2×10^{24} m^{-3}), which corresponds to a cluster containing a single atom with all first and second nearest neighbor Cu atoms and a radius of 0.29 nm. An additional 45 clusters contain at least 9 Cu atoms (atom + all first nearest neighbors), while 9 clusters contain 23 or more atoms (number density of 3.8×10^{23} m^{-3}). This KLMC simulation is currently continuing to reach higher doses. However, the initial results are consistent with experimental observations and show

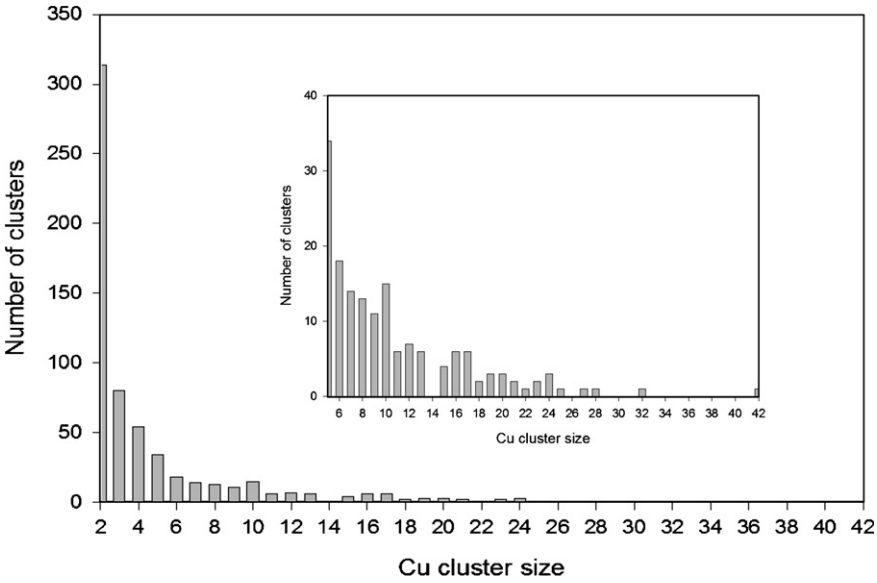

Fig. 3. Cu cluster size distribution obtained at 5.34 Mdpa (Fig. 2f) and 290 °C, at a nominal dose rate of 10^{-11} dpa/s and a vacancy introduction rate of 10^{-4} s^{-1}.

the formation of a high number density of Cu atom clusters, along with the continual formation and dissolution of three-dimensional vacancy Cu clusters.

Figs. 4 and 5 show a comparison of varying the dose rate from 10^{-9} to 10^{-13} dpa/s at a temperature of 290 °C and a fixed vacancy introduction rate of 10^{-4} s^{-1}. The effect of increasing dose rate is shown in Fig. 4 at an accumulated dose of 1.9 Mdpa, and is especially pronounced when comparing Fig. 4(c) (10^{-13} dpa/s) with Fig. 4(a) (10^{-11} dpa/s) and Fig. 4(b) (10^{-9} dpa/s). At the highest dose rate, a substantially higher number density of small three-dimensional vacancy clusters is observed, which are often complexed with one or more Cu atoms. Vacancy cluster nucleation occurs during cascade aging (as described in Fig. 1) and is largely independent of dose rate, but cluster growth is dictated by the cluster(s) thermal lifetime at 290 °C versus the arrival rate of additional vacancies, which is a strong function of the damage rate and vacancy supersaturation under irradiation. Thus, the higher dose rates produce a larger number of vacancies arriving at the vacancy cluster sinks, resulting in the noticeably larger number of growing vacancy clusters. As well, there is a corresponding decrease in the amount of Cu removed from solution by vacancy diffusion. Fig. 5(a) shows the Cu cluster size distribution at 1.9 Mdpa, while Fig. 5(b) shows the free Cu concentration as a function of dose and dose rate. At 1.9 Mdpa, nearly 0.23% of the initial 0.3% Cu remains in solution, compared to <0.2% (10^{-11} dpa/s) and <0.15% (10^{-13} dpa/s), and both the number and size of the Cu atom clusters is greatly reduced.

In contrast, the effect of decreasing dose rate, at the same vacancy introduction rate, is to greatly accelerate Cu precipitation. Already at 1.9 Mdpa, a number of large Cu atom clusters exist at a dose rate of 10^{-13} dpa/s, with the largest containing 35 Cu atoms, as shown in Figs. 4(c) and 5(a). The removal rate of free Cu from the supersaturated solution in the Fe matrix is also considerably faster, as shown in Fig. 5(b). The increased Cu clustering caused by a decrease in dose rate results from a reduction in the number of cascade vacancy clusters which serve as vacancy sinks. Thus, a higher number of free or isolated vacancies are available to enhance Cu diffusion required for the clustering and precipitation of copper. While these flux effects are anticipated and have been predicted in rate theory calculations performed by Odette and co-workers [27,28], the spatial dependences of cascade production and microstructural evolution, in addition to correlated diffusion and clustering processes involving multiple vacancies and atoms are more naturally modeled and visualized using the KLMC approach.

Future simulations will seek to extend the total dose and evaluate the effect of parameters associated with vacancy migration, and the rate of cascade and free vacancy introduction, which control the balance

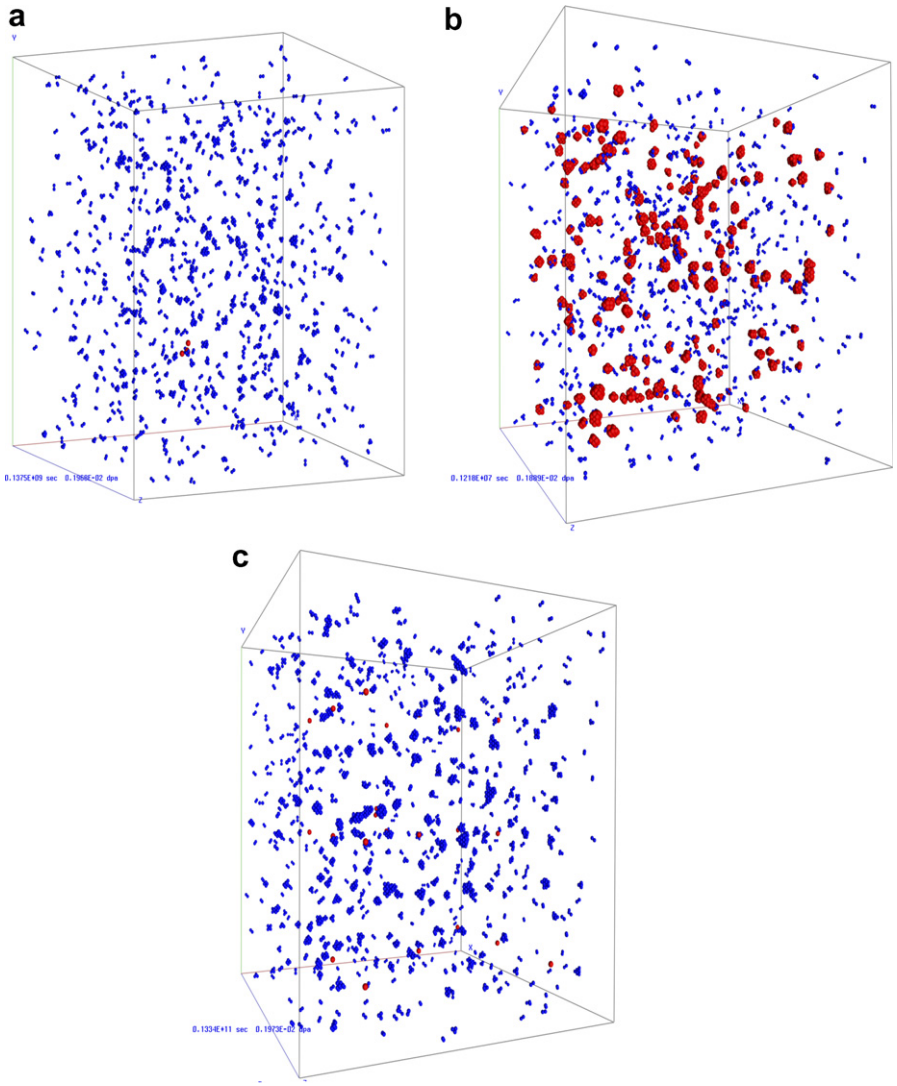

Fig. 4. Comparison of the representative vacancy (red) and clustered Cu atom (blue) population at a dose of ~1.9 Mdpa and 290 °C as a function of dose rate, at (a)10^{-11} dpa/s, (b)10^{-9} dpa/s, (c) 10^{-13} dpa/s.

of microstructural evolution between copper clustering and precipitation and cascade vacancy–solute clusters. As well, the statistics associated with the Cu precipitation and vacancy–Cu cluster distributions will be assessed as a function of simulation parameters and irradiation variables. Further, with the ability to extend the KLMC simulations to higher doses, the simulation results can also be compared with an experimental database of Cu precipitate evolution in Fe–Cu model alloys as a function of irradiation dose, dose rate and temperature. The UCSB experimental database on Cu precipitate evolution, including data obtained from SANS and other characterization techniques, as well as positron annihilation spectroscopy results on the vacancy cluster number density and size, will be used. Such comparisons will validate the KLMC modeling approach and the parameters within the model.

4. Summary and future work

This paper describes the development of a kinetic lattice Monte Carlo model to simulate the long-term evolution of neutron irradiated Fe–Cu alloys. The model simulates the vacancy–copper atom evolution as a result of individual vacancy jumps to nearest neighbor positions, based on the energy change in switching configurations calculated from Finnis–Sinclair type potentials on a fixed lattice. In addition to the diffusion of vacancy and Cu atoms, algo-

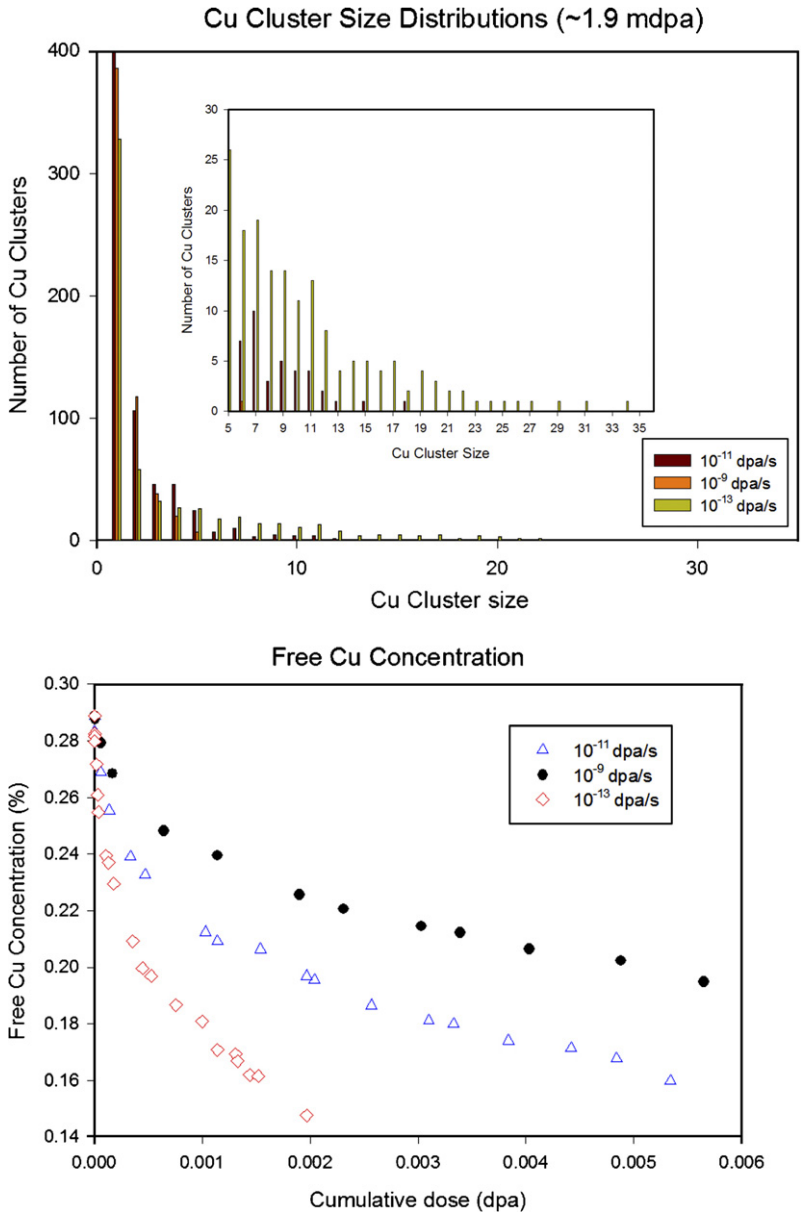

Fig. 5. (a) Cu cluster size distribution at ~1.9 Mdpa for different dose rates, (b) free Cu concentration as a function of cumulative dose for different dose rates.

rithms have been developed to introduce additional displacement damage, including self-interstitial atom–vacancy recombination, and to introduce a flux of diffusing vacancies due to the supersaturated vacancy concentrations under irradiation. These algorithms enable modeling of the wide range of timescales inherent to irradiation-induced nanostructural evolution at low dose rates.

The results of initial KLMC model simulations of damage accumulation in an Fe–0.3% Cu alloy at 290 °C and irradiation dose rates of 10^{-9}, 10^{-11} and 10^{-13} dpa/s are presented and reveal the continuous formation and dissolution of three-dimensional vacancy–Cu clusters from the remnants of the vacancy-rich displacement cascade core, in addition to the formation of a high number density of copper clusters that grow with increasing irradiation dose. The effect of increasing dose rate is to retard Cu diffusion and precipitation and to increase the population of vacancy clusters, consistent with

expectation and experiment. To our knowledge, these simulation results represent the first time that a kinetic Monte Carlo model has successfully demonstrated both Cu precipitate formation and vacancy–Cu cluster formation, as experimentally observed. Future modeling efforts will evaluate the effect of the parameters used in the model, perform multiple simulations to provide statistics associated with the evolutions, and quantitatively compare the results to available experimental data.

Acknowledgements

This work has been partially supported at UCB by the Office of Fusion Energy Sciences, US Department of Energy, under Grant DE-FG02-04ER54750 and at UCSB by the US Nuclear Regulatory Commission under Contracts #04-94-049 and 04-01-064.

References

[1] G.R. Odette, Materials Research Society Symposium Proceedings, vol. 373, Materials Research Society, Warrendale, Pennsylvania, 1995, p. 137.
[2] G.R. Odette, G.E. Lucas, Radiat. Eff. Defect. Solids 144 (1998) 189.
[3] G.R. Odette, G.E. Lucas, JOM 53 (2001) 18.
[4] G.R. Odette, Neutron Irradiation Effects in Reactor Pressure Vessel Steels and Weldments, IAEA IWG-LMNPP-98/3, International Atomic Energy Agency, Vienna, 1998, p. 438.
[5] G.R. Odette, B.D. Wirth, D.J. Bacon, N.M. Ghoneim, MRS Bull. 26 (2001) 176.
[6] G.R. Odette, T. Yamamoto, D. Klingensmith, Philos. Mag. 85 (2005) 779.
[7] G.S. Was, M. Hash, G.R. Odette, Philos. Mag. 85 (2005) 703.
[8] G.R. Odette, B.D. Wirth, J. Nucl. Mater. 251 (1997) 157.
[9] A. Ulbricht, J. Boehment, P. Strunz, C. Dewhurst, M.H. Mathon, Appl. Phys. A – Mater. Sci. Process. 74 (2002) S1128.
[10] M. Grosse, J. Boehment, R. Gilles, J. Nucl. Mater. 254 (1998) 143.
[11] B.D. Wirth, G.R. Odette, P. Asoka-Kumar, R.H. Howell, P.A. Sterne, in: G.S. Was (Ed.), Proceedings of the 10th International Symposium on Environmental Degradation of Materials in Light Water Reactors, National Association of Corrosion Engineers, 2002.
[12] M.K. Miller, B.D. Wirth, G.R. Odette, Mat. Sci. Eng. A 353 (2003) 133.
[13] P. Pareige, K.F. Russel, R.E. Stoller, M.K. Miller, J. Nucl. Mater. 250 (1997) 176.
[14] M.K. Miller, P. Pareige, M.G. Burke, Mater. Charact. 44 (2000) 235.
[15] P. Auger, P. Pareige, S. Welzel, J.C. Van Duysen, J. Nucl. Mater. 280 (2000) 331.
[16] G.R. Odette, C. Cowan, in: G.S. Was (Ed.), Proceedings of the 10th International Symposium on Environmental Degradation of Materials in Light Water Reactors, National Association of Corrosion Engineers, 2002.
[17] S. Ishino, Y. Chimi, Bagiyono, T. Tobita, N. Ishikawa, M. Suzuki, A. Iwase, J. Nucl. Mater. 323 (2003) 354.
[18] Y. Nagai, M. Hasegawa, Z. Tang, A. Hempel, K. Yubuta, T. Shimamura, Y. Kawazoe, A. Kawai, F. Kano, Phys. Rev. B 61 (2000) 6574.
[19] Y. Nagai, Z. Tang, M. Hasegawa, T. Kanai, M. Saneyasu, Phys. Rev. B 63 (2001) 134110.
[20] P. Asoka-Kumar, B.D. Wirth, P.A. Sterne, G.R. Odette, Philos. Mag. Lett 82 (2002) 609.
[21] S.C. Glade, B.D. Wirth, G.R. Odette, P. Asoka-Kumar, P.A. Sterne, R.H. Howell, Philos. Mag 85 (2005) 629.
[22] M. Hasegawa, Z. Tang, Y. Nagai, T. Chiba, E. Kuramoto, M. Takenaka, Philos. Mag 85 (2005) 467.
[23] G.R. Odette, E.V. Mader, G.E. Lucas, W.J. Phythian, C.A. English, The effects of radiation on materials, 16th Int. Symp, ASTM-STP-1175, American Society for Testing and Materials, Philadelphia, PA, 1993, p. 373.
[24] G.R. Odette, B.D. Wirth, Radiation effects in fission and fusion reactors, in: Handbook of Materials Modeling. Volume I: Methods and Models, Springer, Netherlands, 2005. Article 2.29.
[25] B.D. Wirth, G.R. Odette, MRS Soc. Symp. Proc. 481 (1998) 151.
[26] C. Domain, C.S. Becquart, J.C. Van-Duysen, MRS Soc. Symp. Proc. 540 (1999) 643.
[27] M.J. Caturla, N. Soneda, E.A. Alonso, B.D. Wirth, T. Diaz de la Rubia, J. Nucl. Mater. 276 (2000) 13.
[28] B.D. Wirth, G.R. Odette, R.E. Stoller, MRS Soc. Symp. Proc 677 (2001) AA5.2.
[29] R.E. Stoller, MRS Soc. Symp. Proc. 373 (1995) 21.
[30] R.E. Stoller, L.R. Greenwood, J. Nucl. Mater. 272 (1999) 57.
[31] R.E. Stoller, personal communication.
[32] B.K.P. Chang, B.D. Wirth, unpublished results.
[33] M.W. Finnis, J.E. Sinclair, Philos. Mag. A 50 (1) (1984) 45.
[34] G.J. Ackland, G.I. Tichy, V. Vitek, M.W. Finnis, Philos. Mag. A 56 (1987) 735.
[35] B.D. Wirth, G.R. Odette, MRS Soc. Symp. Proc. 481 (1998) 151.
[36] M.P. Allen, D.J. Tildesley, Computer Simulation of Liquids, Clarendon, Oxford, 1990.
[37] L.R. Greenwood, R.K. Smither, SPECTER: Neutron Damage Calculations for Materials Irradiations, ANL/FPP/TM-197, Argonne National Laboratory, Argonne, IL, 1985.
[38] M.T. Robinson, J. Nucl. Mater. 216 (1994) 1.
[39] ASTM E521-96, in: Standard Practices for Neutron Radiation Damage Simulation by Charged-Particle Irradiation, Annual Book of ASTM Standards, vol. 12.02, American Society of Testing and Materials, Philadelphia, PA, 2003.
[40] J. Marian, B.D. Wirth, J.M. Perlado, G.R. Odette, T. Diaz de la Rubia, Phys. Rev. B 64 (2001) 094303.
[41] A.F. Calder, D.J. Bacon, J. Nucl. Mater. 207 (1993) 25.
[42] B.D. Wirth, G.R. Odette, D. Maroudas, G.E. Lucas, J. Nucl. Mater. 244 (1997) 185.
[43] Y.N. Osetsky, A. Serra, V. Priego, J. Nucl. Mater. 276 (2000) 202.
[44] R.E. Stoller, The effects of radiation on materials, 16th Int. Symp, ASTM-STP-1175, American Society for Testing and Materials, Philadelphia, PA, 1993, p. 394.
[45] C. Domain, C.S. Bequart, Phys. Rev. B 65 (2002) 024103.
[46] C.-C. Fu, F. Willaime, P. Ordejon, Phys. Rev. Lett. 92 (2004) 175503.